Crystal structure and functional mechanism of a human antimicrobial membrane channel

Chen Song[a], Conrad Weichbrodt[b], Evgeniy S. Salnikov[c], Marek Dynowski[d,e], Björn O. Forsberg[a], Burkhard Bechinger[c], Claudia Steinem[b], Bert L. de Groot[a], Ulrich Zachariae[f,1], and Kornelius Zeth[e,g,1]

[a]Computational Biomolecular Dynamics Group, Max Planck Institute for Biophysical Chemistry, 37077 Göttingen, Germany; [b]Institute for Organic and Biomolecular Chemistry, Georg August University Göttingen, 37077 Göttingen, Germany; [c]Membrane Biophysics and NMR, Chemistry Institute, Unité Mixte de Recherche 7177, University of Strasbourg and Centre National de la Recherche Scientifique, 67000 Strasbourg, France; [d]Research and Development, Computing Centre, Freiburg University, 79104 Freiburg, Germany; [e]Max Planck Institute for Developmental Biology, 72076 Tübingen, Germany; [f]Scottish Universities' Physics Alliance, School of Physics and Astronomy, The University of Edinburgh, Edinburgh EH9 3JZ, United Kingdom; and [g]Unidad de Biofisica, University of Basque Country and Spanish Science Research Council, 48940 Leioa, Vizcaya, Spain

Edited by Wolfgang Baumeister, Max-Planck Institute of Biochemistry, Martinsried, Germany, and approved January 16, 2013 (received for review August 28, 2012)

Multicellular organisms fight bacterial and fungal infections by producing peptide-derived broad-spectrum antibiotics. These host-defense peptides compromise the integrity of microbial cell membranes and thus evade pathways by which bacteria develop rapid antibiotic resistance. Although more than 1,700 host-defense peptides have been identified, the structural and mechanistic basis of their action remains speculative. This impedes the desired rational development of these agents into next-generation antibiotics. We present the X-ray crystal structure as well as solid-state NMR spectroscopy, electrophysiology, and MD simulations of human dermcidin in membranes that reveal the antibiotic mechanism of this major human antimicrobial, found to suppress *Staphylococcus aureus* growth on the epidermal surface. Dermcidin forms an architecture of high-conductance transmembrane channels, composed of zinc-connected trimers of antiparallel helix pairs. Molecular dynamics simulations elucidate the unusual membrane permeation pathway for ions and show adjustment of the pore to various membranes. Our study unravels the comprehensive mechanism for the membrane-disruptive action of this mammalian host-defense peptide at atomistic level. The results may form a foundation for the structure-based design of peptide antibiotics.

crystallography | electrophysiology | ion conduction | molecular dynamics

Host-defense peptides actively control a wide range of microbes across most tissues of the animal and plant kingdoms, which signifies their importance during the evolution of multicellular organisms (1–3). In comparison with traditional small-molecule antibiotics, host-defense or antimicrobial peptides (AMPs) are often considered to have a distinctly superior property, as they target the microbial Achilles heel, i.e., the unique but essential features of all microbial cellular membranes (albeit at somewhat lower efficacy) (1–5). Thus, microbes have not been able to develop efficient resistance mechanisms against AMPs within the time frame of their parallel evolution (3, 5).

In recent years, a steep global rise in infections by multiresistant bacteria such as methicillin-resistant *Staphylococcus aureus* (MRSA) has been recorded (6, 7). These often affect the patients' skin and epithelial injuries, and are particularly hard to treat with conventional small-molecule antibiotics (8). The development of high-efficiency antibiotic agents, less prone to evoking resistance, is thus essential (4–7). However, the rational design of AMPs requires a detailed understanding of their structural and mechanistic determinants of antimicrobial action, which has not been achieved to date (4, 9, 10). The lack of molecular-based understanding has been named as the main obstacle hampering progress in this field (11).

The human epithelium exposes a large external surface for the growth of microbes (12). Among the major AMPs detected on human skin is the negatively charged peptide dermcidin (DCD; refs. 13–15), which is constitutively produced in sweat glands as a precursor protein, further processed and finally secreted into human sweat (refs. 13 and 16; Fig. S1 *A–C*). DCD is active against a broad spectrum of bacteria including MRSA and rifampin- and isoniazid-resistant *Mycobacterium tuberculosis* at concentrations of ~1 μg/mL (16). Its antimicrobial activity is particularly robust against changes in pH and ionic strength (13, 16). When isolated from sweat or after recombinant expression, DCD forms an equilibrium mixture of oligomers of varying size, both in solution and in membrane mimetics (16, 17). Human sweat is enriched in divalent ions, among which Zn^{2+} is of particular importance and has previously been demonstrated to be essential for AMP action on some microbes (18, 19).

AMPs are classified according to their overall charge, secondary structure, and more specifically the presence of certain amino acid combinations such as cysteines or prolines (1, 9). Many AMPs carry an excess of positive charges to interact favorably with the negatively charged surface of bacterial membranes (1–3). Although a number of models for the membrane-disrupting action of AMPs have been proposed, detailed and compelling structural and mechanistic evidence for any of these models involving mammalian (or human) AMPs has so far been elusive (4, 9, 10). To elucidate the antibiotic mechanism of DCD and reveal the underlying structural determinants, including the level of oligomerization, we crystallized the 48-residue DCD peptide (Fig. S1*A*), determined its channel-forming structure, and looked at membrane interaction with solid-state (ss) NMR spectroscopy. We then conducted electrophysiology experiments in which we characterized the activity of DCD in membranes under various conditions. The experimental results are in excellent agreement with data we obtained from extended computational electrophysiology and molecular dynamics (MD) simulations of the channel assembly, which further reveal the ion-transfer mechanism of DCD in atomic detail.

Results

Structural Architecture of the Hexameric AMP Channel. The structure of assembled DCD solved at 2.5-Å resolution exhibits a channel architecture comprising a hexameric bundle formed by

Author contributions: C. Song, B.B., C. Steinem, B.L.d.G., U.Z., and K.Z. designed research; C. Song, C.W., E.S.S., M.D., B.O.F., and K.Z. performed research; C. Song, C.W., E.S.S., B.O.F., B.B., C. Steinem, B.L.d.G., U.Z., and K.Z. analyzed data; and C. Song, E.S.S., B.B., C. Steinem, B.L.d.G., U.Z., and K.Z. wrote the paper.

The authors declare no conflict of interest.

This article is a PNAS Direct Submission.

Freely available online through the PNAS open access option.

Data deposition: The atomic coordinates and structure factors have been deposited in the Protein Data Bank, www.pdb.org (PDB ID code 2YMK).

[1]To whom correspondence may be addressed. E-mail: uzachari@ph.ed.ac.uk or kornelius.zeth@googlemail.com.

This article contains supporting information online at www.pnas.org/lookup/suppl/doi:10.1073/pnas.1214739110/-/DCSupplemental.

elongated α-helices, which adopts overall dimensions of ~8 × 4 nm (Fig. 1*A*). Channel formation involves trimerization of antiparallel peptide dimers resulting in a firmly enclosed channel structure. Each monomer presents two distinct interfaces to neighboring subunits (Fig. 1*A*). The extended interface, displaying a contact surface of 930 Å^2, is mainly formed by salt bridges, and the second interface covers 520 Å^2 (IF1) and is primarily stabilized by Zn^{2+} ions that intercalate between the two helices (Fig. 1*A* and Fig. S1*D*). The zinc ions in DCD are coordinated by *N*- and C- terminal residues of dimerizing peptides (residues involved: Glu5, Glu9, His38′, and Asp42′) (Fig. 1 *A* and *B*). They are attached to the inner wall of the channel and substantially change the overall charge of the assembly (from −12*e* to neutral). In addition, they modify the local charge distribution especially at the entrance of the channel.

DCD shows a unique distribution of charges, reflecting peptide oligomers that occur both in soluble and membrane-bound forms. The entire hexameric channel comprises 96 ionizable residues, which are all oriented toward the channel interior (Fig. 1 *C, F,* and *G*). This enormous charge density, which is not completely shielded to the exterior, is likely to contribute to the relatively high aqueous solubility of DCD. The inner space of the peptide channel has an apparent separation into five radially symmetric charge girdles I/II/III/II/I (Fig. 1*C*). Residues facing the acyl chain region of the membrane are exclusively hydrophobic (Ala, Val, Leu) (Fig. 1*D* and Fig. S1*A*). However, no aromatic residues are found that are commonly considered to be important for the lateral adjustment of proteins in membranes (20, 21). The channel diameter is not homogeneous and varies along the *y* axis with two rather narrow entry sites, followed by a widened interior with windowlike eyelets in the IF1 interface (Fig. 1 *A, E,* and *H*). The six lateral openings have a diameter of ~1 nm and are surrounded by small amino acids as well as positively charged residues that may have an influence on the selection of ion entry. The distance between two adjacent eyelets is 2.5 (same plane) and 3 nm (opposite plane), respectively, roughly corresponding to the width of the membrane hydrophobic core.

Interaction of DCD with Lipid Bilayers. To investigate the interaction of DCD with bilayers, we conducted ss-NMR spectroscopy experiments. The structural preferences of DCD were investigated after labeling of the peptide with ^{15}N at the Gly22 position and $^2H_3$-Ala at position 25, its reconstitution into oriented lipid bilayers and investigation by proton-decoupled ^{15}N ss-NMR spectroscopy. DCD labeled with ^{15}N at Gly22 exhibits a ^{15}N chemical shift of (62 ± 2) ppm in oriented 1-palmitoyl-2-oleoyl-*sn*-glycero-3-phosphoethanolamine/1-palmitoyl-2-oleoyl-

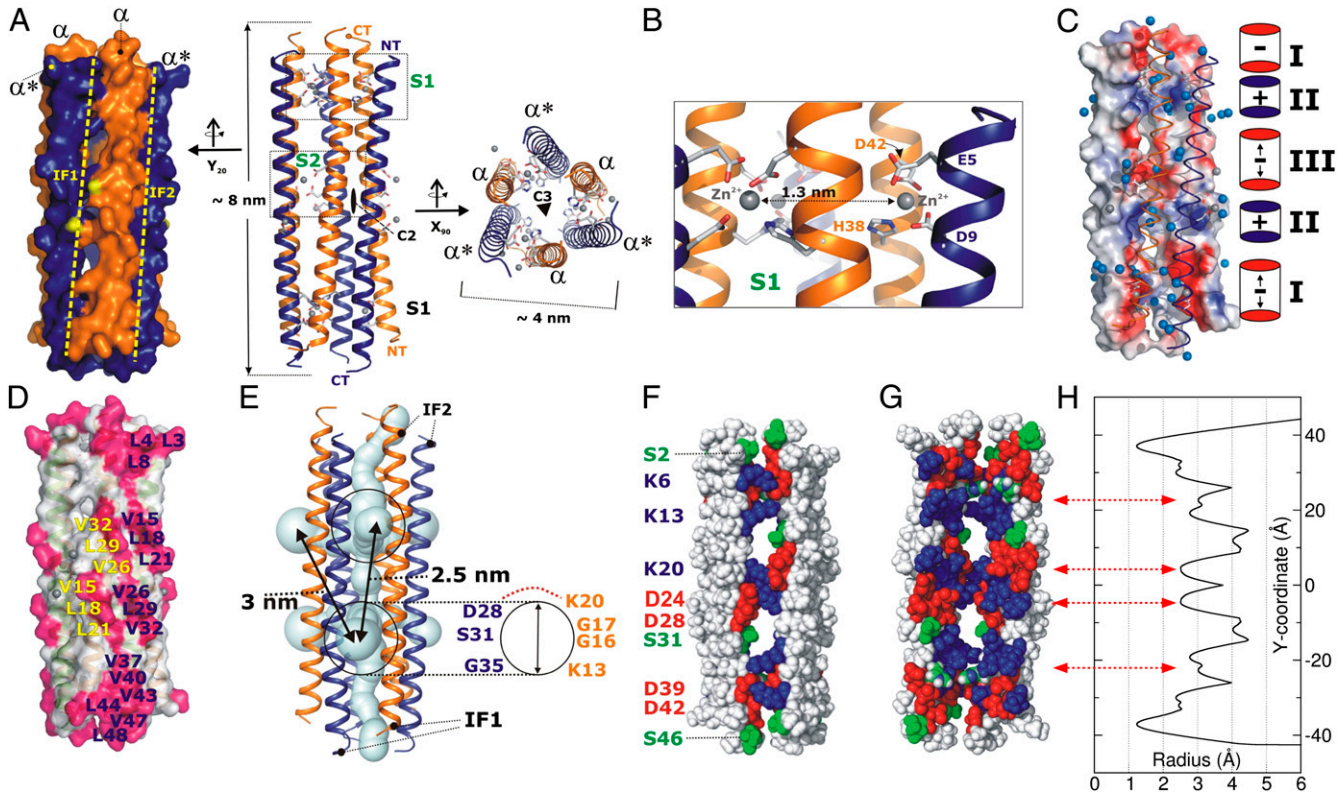

Fig. 1. Crystal structure and surface characteristics of the human dermcidin channel. (*A*) X-ray structure of the hexameric DCD channel shown in cartoon representation from the side and top (*Middle* and *Right*), and as surface representation (*Left*). The different orientations of the individual peptides relative to the membrane normal are marked in orange and dark blue, and termini are marked (NT, N terminus; CT, C terminus). Arrows combined with tilt angle and axes give the relative orientation. Residues involved in Zn binding are shown in stick representation and Zn ions are marked in gray. The symmetry axis of the channel is marked with C2 (for the side view) and C3 (for the top view). Two interfaces of different surface area are formed after trimerization and named IF1 and IF2. (*B*) Close-up into the Zn-binding site S1. Four residues (Glu5 and Asp11 from one peptide and Asp41 and His38 from the second) form each Zn-binding site. The distance between the Zn ions is marked by arrows. (*C*) Electrostatic surface representation of the channel with two monomers marked in ribbon representation. The channel comprises five alternating patches of elongated negative (red) and ring-like positive (blue) charge. (*D*) Side view of DCD (hydrophobic residues in magenta). (*E*) Ribbon model of DCD. The pore diameter is represented by spheres. The lateral entry points are marked with circles. (*F*) Hydrophilic residues on the trimeric interface (negatively charged residues in red, positively charged residues in blue, polar residues in green). Nonpolar residues are shown in white. (*G*) The hydrophilic channel interior. For clarity, the front dimer is omitted; colors as in *F*. (*H*) Channel radius along the pore axis.

sn-glycero-3-phospho(1'-rac-glycerol) (POPE/POPG, 3:1) membranes both in the absence or presence of a 10-fold excess of Zn^{2+} (Fig. 2 *A* and *B*). This indicates an in-planar alignment of the major population of the labeled peptide domain (22), in agreement with previous oriented circular dichroism data (16). The chemical shifts are within experimental error identical in POPE/POPG, 1-palmitoyl-2-oleoyl-*sn*-glycero-3-phosphocholine, and DPhPC/cholesterol 9:1 membranes and also independent of zinc ions ($ZnCl_2$ salt) and the sample preparation protocol. The ^2H ss-NMR spectrum of the $^2H_3$-Ala25 labeled site exhibits an ^2H quadrupolar splitting of (45 ± 3) kHz (Fig. 2*C*) and further restricts the tilt and pitch angle (23). A detailed topological analysis is shown by the red and black traces in Fig. S2 for the ^{15}N chemical shift and the ^2H quadrupolar splitting, respectively (see ref. 23). Both NMR parameters agree when their corresponding traces intersect leading to a set of tilt/pitch angular pairs in the proximity of (90°/90°), which would represent an ideal alignment of the amphipathic helix with the membrane interface (Fig. 2*B*). In agreement, the ^2H spectra of the fatty acyl chains show pronounced membrane disordering by the presence of DCD (Fig. S3).

Functional Properties of the Channel Highlight the Importance of Zinc as Cofactor. The solid-state NMR data represent probably the lowest energy state after extensive equilibration of the major population of the peptide and, in particular, in the absence of a membrane potential. In contrast, electrophysiological recordings monitor a population that may occur as a minor, but functionally relevant, species under the application of a transmembrane voltage. To obtain functional evidence for the activity of DCD channels in the membrane, we collected conductivity data in planar lipid bilayers. First, membranes were prepared in 1 M NaCl, 5 mM Hepes, pH 7.1 in the absence of Zn^{2+}. After the addition of DCD in micromolar concentrations, two out of the six membranes showed weak activity of the peptide (Fig. 2*D*). Altogether, only 20 current steps were observed, from which a mean conductance of $G = (31 \pm 8)$ pS was evaluated.

By contrast, in the presence of Zn^{2+}, the addition of DCD at concentrations of 850 nM or higher resulted in current fluctuations for every membrane preparation, which eventually led to rupture of the membrane (Fig. 2 *E* and *F*). These concentrations are similar to DCD concentrations used to efficiently remove bacteria in antimicrobial assays. Evaluation of 1,009 events revealed a mean conductance of $G = (81 \pm 14)$ pS (Fig. 2*G*) and the mean open lifetime was determined to be $\tau = (4.4 \pm 0.2)$ ms (Fig. 2*H*). This shows that, in the presence of zinc ions, specific and individual channels with a defined conductance are formed in the membrane bilayer. Neither the membrane with DCD alone nor the addition of only Zn^{2+} gave rise to the occurrence of individual channels in the electrophysiology experiments. However, we found that the polarity of the electric field had a significant impact on the efficiency of DCD-Zn^{2+} insertion.

To further investigate the importance of the specific Zn^{2+} interactions and their impact on the active membrane-bound form of DCD, we mutated His38, one of the main interaction partners of DCD with Zn^{2+}, to alanine and studied this mutant through electrophysiology. The single mutation was sufficient to abolish channel formation in membranes (Fig. S4). This finding is most compatible with the notion that the assembled structure, which is characterized by specific Zn^{2+}-conferred peptide–peptide interactions, is the most prominent membrane-disruptive form. It is important to note that the current fluctuations seen for DCD-Zn^{2+} in electrophysiology are representative of a small number of channels efficiently conducting ions across membranes,

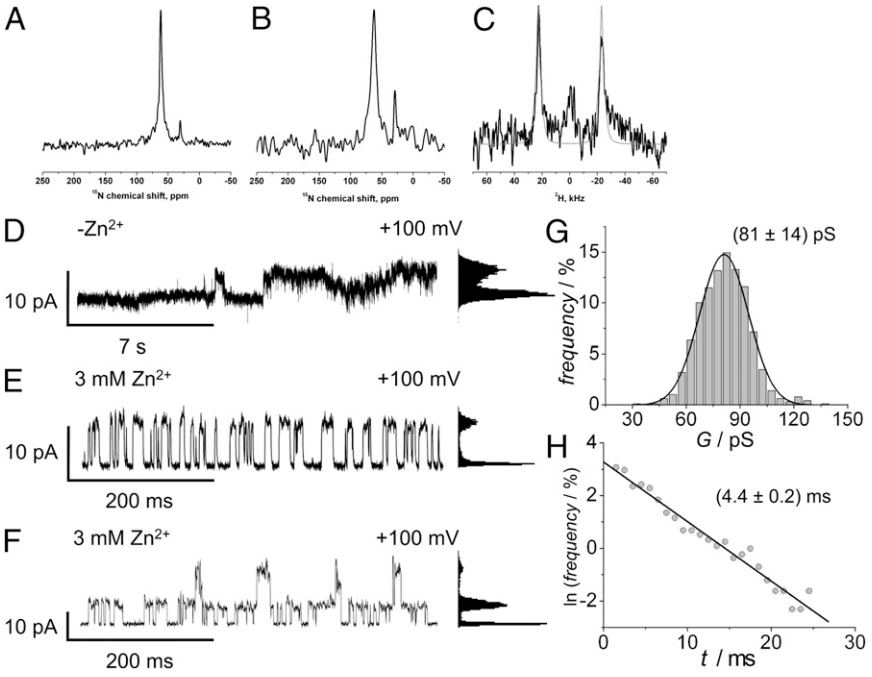

Fig. 2. Electrophysiology and ss-NMR of DCD in the presence and absence of zinc ions. (*A* and *B*) Proton-decoupled ^{15}N and (*C*) ^2H ss-NMR spectra of 2 mol % [^{15}N-Gly22,$^2H_3$-Ala25]-DCD in oriented POPE/POPG without $ZnCl_2$ (*A*) and with fivefold molar excess of $ZnCl_2$ relative to the peptide concentration (*B* and *C*). $^{15}NH_4Cl$ (40.0 ppm) and ^2H_2O (0 Hz) were used as external references and the spectra processed with an exponential line broadening of 50 (*A* and *B*) and 500 Hz (*C*), respectively. The gray line in *C* shows a simulated spectrum arising from a 3° Gaussian distribution for the peptide alignment and a spectral line width of 2 kHz. (*D*) Current trace and point amplitude histogram representing DCD activity in 1 M NaCl, 5 mM Hepes, pH 7.1 recorded at a holding potential of +100 mV. Protein activity was only rarely observed under these conditions. (*E* and *F*) Current traces and point amplitude histograms of DCD-1L in 1 M NaCl, 3 mM $ZnCl_2$, 5 mM Hepes, pH 7.1 recorded at a holding potential of +100 mV; (*E*) 3.3 μM DCD-1L was added resulting in one defined conductance state. In (*F*) 7.9 μM DCD-1L was used and two distinct conductance levels each of about 80 pS were monitored, suggesting the insertion of two channels. (*G*) An event histogram of the conductance levels (n = 1,009) shows a mean conductance of $G = (81 \pm 14)$ pS. (*H*) Open lifetime analysis with $\tau = (4.4 \pm 0.2)$ ms.

whereas the ss-NMR measurements observe the major peptide fraction only.

Molecular Dynamics Simulations Reveal Unexpected Ion-Transfer Pathways. To obtain a detailed mechanistic picture of DCD acting on membranes, we performed extensive atomistic MD simulations of the DCD channel in negatively charged, bacterial-like phosphatidyl ethanolamine/ phosphatidyl glycerol (POPE/POPG, 3:1) bilayers (24), and carried out computational electrophysiology simulations to monitor its ion permeation properties (Fig. S5). The DCD assembly including Zn^{2+} exhibited a high level of structural stability in membranes (C-α root-mean-square deviation ~2 Å; Fig. S6). In aqueous solution, the aggregate was found to be stable, but showed a markedly raised structural variability (Fig. S6*B*). Consistent with our experimental data, removal of the Zn^{2+} ions from the membrane-inserted assembly structure resulted in a substantial distortion of the oligomer, compromising its membrane-channel character (Fig. S6*D*). These findings agree well with previous NMR studies, in which both a membrane-mimetic solvent (TFE-$^2H_3$) and Zn^{2+} were shown to induce oligomerization of DCD (16).

After initially positioning the complex normal to the bilayer plane, the assembly adopted tilted configurations relative to the membrane normal within 250 ns simulated time (γ~30°; Fig. 3*A*). The inclination was found to compensate for the hydrophobic mismatch between the bilayer and the hydrophobic region on the outer surface of DCD, and its magnitude depended on the length of the surrounding lipids (Fig. S7*A*).

During the simulations, the interior of the oligomer rapidly filled with water and formed a permanent water channel across the membrane (Fig. 3 *B* and *C*). Water also partitioned into the three hydrophilic crevices at the trimer interfaces, such that a high osmotic water permeability coefficient of $(327 \pm 13) \times 10^{-14}$ $cm^3 \cdot s^{-1}$ was determined that exceeds that of aquaporin channels by up to 50-fold (25). To investigate the conductivity of DCD for ions, we used computational electrophysiology to model biologically realistic electrochemical gradients across membranes (26). At 1 M NaCl concentration, we obtained a DCD channel conductance of (108 ± 11) pS, in excellent agreement with our experimental data (Figs. 2*G* and 3*D*). In simulations at a salt concentration of 150 mM, a total single-channel conductance of (50 ± 7) pS was obtained (Fig. 3*D*). In all of our simulations, DCD showed pronounced anion selectivity (Fig. S7*B*).

The remarkable agreement between computational and experimental data strongly suggests that the hexameric crystal structure is identical to the functional state in the membranes used for electrophysiology. Any higher or lower oligomerization state of DCD would very likely lead to markedly different conductance values (*SI Materials and Methods* and Fig. S8). This interpretation is corroborated by the strong dependence of channel current on zinc, which we observed in both the electrophysiology experiments and MD simulations in membranes, and which corresponds with the abundance and function of the Zn^{2+} binding sites, linking the subunits in the crystal structure.

It is notable that DCD exhibited a unique ion-permeation pathway in the simulations, which offers an explanation for this unexpectedly high conductance (Movies S1 and S2), despite its limited channel cross-section. Through channel tilt, ions are capable of entering sideways into the pore across the eyelets that occur at the trimeric interfaces. This not only shortens the pathway across the channel, but importantly, exploits the increased ion concentration observed at the lipid head groups by enabling these ions to enter the channel directly, and to rapidly traverse the inner pore (Fig. 3*C* and Movies S1 and S2). Also within the channel, DCD shows an unusual anion traversal mechanism. Most anion transfer steps across the inner section of the pore consist of single ion "hopping" transitions. Near the channel termini, however, anions accumulate to form clusters of three or four ions, most clearly seen at the channel exit. Productive ion translocations exiting the channel usually involve multiion "knock-on" effects, through which individual anions are expelled from this cluster to the bulk solution (Movie S1).

The stabilization of DCD oligomers by a membrane mimetic, seen in earlier NMR studies (16), is also corroborated by molecular dynamics simulations, in which we tested the long-term stability of the DCD assembly in a membrane environment vs. aqueous solution. Fig. S6*B* shows that the assembled structure with Zn^{2+} shows a substantially raised stability in bilayers relative to solution, which indicates a preference of the hexameric assembly for the membrane environment.

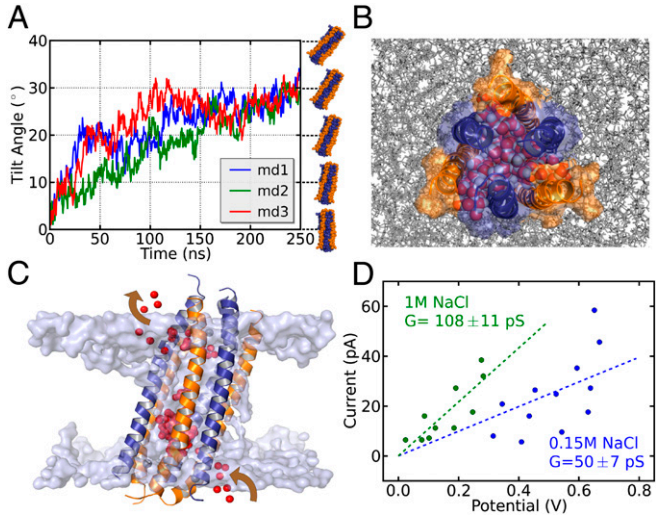

Fig. 3. Computational electrophysiology and molecular dynamics simulations of the channel. (*A*) Evolution of DCD tilt in three 250-ns single-bilayer MD simulations in POPE/POPG(3:1). (*B*) Water distribution (red/white spheres) in and around the DCD channel in the bilayer (gray); view along the channel axis. (*C*) Pathway of ion permeation. One complete Cl^- permeation event is shown, with red spheres representing snapshots of Cl^- position. The brown arrows indicate the direction of permeation. (*D*) The I–V relationships from computational electrophysiology simulations. Each data point was obtained from a 100-ns MD trajectory by monitoring the number of permeation events (and thus the current) and the overall transmembrane potential during this time window. Blue and green circles are from simulations with 0.15 M and 1 M NaCl in solution, respectively. Dashed lines: linear fit of the conductance data, with the slope (and the asymptotic SE) showing overall conductance.

Discussion

The existence of antimicrobial agents in various secretions of multicellular organisms has been discovered over 100 y ago (9), and to date, more than 1,700 known and putative antimicrobial peptides have been identified (4). Although there has been little doubt that the antimicrobial mechanism of AMPs includes interactions with microbial cell membranes, compelling structural and functional evidence for any of these mechanisms has not yet been achieved, and it is possible that there are a variety of different modes of action (4, 9). High-resolution structural information on the functionally active states of AMPs has so far been limited to agents from microbes, insects, and on β-sheet forming defensins from higher organisms, which form a distinct structural class (14, 27–32). In terms of function, electrophysiological measurements have suggested the formation of wide channels with varying conductance around 2.5 nS for the moth AMP cecropin (33), and of very large-conductance pores for defensin from rabbit (34), however without providing structural information for the assemblies.

Here, we present a comprehensive functional mechanism of a human antimicrobial peptide in its active form, including its high-resolution structure, single-channel functional measurements, and atomistic simulations of permeation. In the absence of transmembrane voltage (TMV), in-plane alignments have been observed for DCD and other helical antimicrobial peptides such as magainins or cecropins (Fig. 2 *A*–*C*; reviewed in ref. 35). However, important differences exist between the latter peptides and DCD, already when their size and charge are compared. Of note is that when TMV is applied, the channel recordings reveal mostly membrane lysis in the case of magainins or cecropins, and only rarely are the stepwise conduction increases clearly observed with DCD. The electrophysiological recordings of lysis or stochastic membrane deformations, however, are erratic, highly variable, and characterized by considerable fluctuations. Therefore, it is likely that the tilted hexamer of DCD provides an example for a hitherto undescribed mechanism for the membrane interactions of antimicrobial peptides (for reviews of other mechanisms, see ref. 36). The ensemble of data from the herein and previously presented studies (16) suggest that DCD occurs in a number of states that are interconnected by sensitive equilibria as illustrated in Fig. 4, including oligomers and monomers in solution, as well as monomers or small oligomers lying parallel to the membrane surface (Fig. 2 *A*–*C*). Furthermore, transmembrane potentials and the presence of Zn^{2+}, by neutralizing the anionic charges of the DCD polypeptides, favor the formation of oligomeric structures spanning the membrane (Fig. 2 *D*–*H*). These channels display a conductance of about 80 to 110 pS.

Although the suggested mechanisms of AMP action have so far remained largely speculative (4, 9, 10), our study on DCD provides a structurally detailed and experimentally validated mechanism for membrane perturbation by an AMP. It is striking that none of the currently debated models explicitly predict this channel. Our X-ray, electrophysiology, and simulation data show a barrel-stave–like channel (10), which is held together by divalent cations and displays a high permeability for water and ions, as ions can enter and exit through side eyelets of a tilted pore. DCD thereby forms a site of severe membrane disruption. As recently noted, a single ion channel with a conductance near 100 pS can dissipate the bacterial transmembrane potential on a time scale of as little as 10^{-4} s (37). The DCD channel characterized here thus represents highly efficient channels, and even a few of which are capable of rapidly abrogating the bacterial transmembrane potential that is essential for cell survival. Its structure and functional mechanism may form a foundation for the rational design of antibacterial, peptide-derived drugs that are less liable to evoke resistance.

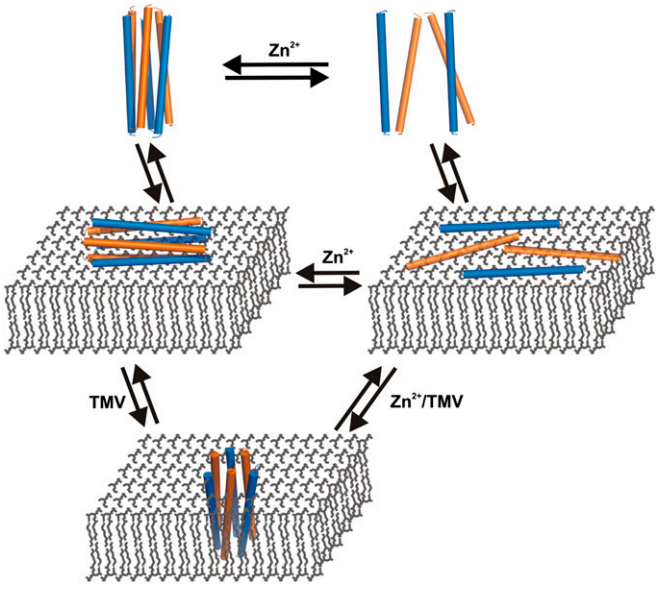

Fig. 4. Model of DCD interactions with membranes. Peptide monomers of DCD are in equilibrium with the hexameric channel form, which is stabilized by the presence of zinc. The channel and DCD monomers can interact with membrane surfaces through lateral association as shown by our NMR studies. The channel can be translocated into the membrane upon application of a TMV, as shown in planar lipid membrane conductance measurements, and forms a representative of the barrel-stave model. Once the channel is integrated into a membrane, channel conductance can be recorded by planar lipid membrane experiments and estimated by molecular dynamics studies.

Material and Methods

Crystallization and Structure Determination. The DCD peptide sequence (Fig. S1) was synthesized by the company Peptide2.0 (www.peptide2.com) to yield a product of >97% purity. For crystallization, the peptide was solved in 10 mM Hepes at a concentration of 50 mg/mL (~10 mM final concentration). Crystallization drops were prepared by mixing 400 nL of the peptide solution with the same amount of reservoir, and drops were incubated by vapor diffusion (sitting drops) under a variety of different conditions (800 conditions from Qiagen screens). Two conditions, both of which contained Zn-acetate, yielded crystals suitable for X-ray diffraction analysis. Crystals for X-ray diffraction were taken from a drop containing 0.2 M $Zn(ac)_2$, 0.1 M Na-cacodylate, 18% (wt/vol) PEG8000 at pH 6.5. The channel has been crystallized in the absence of lipophilic molecules such as detergents or lipids. Crystals were taken from the mother liquor and flash-frozen in liquid nitrogen without adding cryoprotectant. Data were collected at the Swiss Light Source, beamline PXII at 100 K and 20 eV above the theoretical Zn-edge (9.658 keV). Three hundred sixty 1° images were collected at 2% beam intensity to generate a highly redundant dataset for single anomalous dispersion data processing. Diffraction data were processed with XDS/XSCALE (38). The structure was solved with the Phenix program package (39) with Phaser (38) for heavy atom detection and Resolve (40) for initial solvent flattening. Solvent flattening was repeated by Pirate of the CCP4 suite (41) and a model 85% complete was built with Buccaneer (42). The final model was obtained after several rounds of manual rebuilding and refinement with Coot (43), REFMAC (44), and PHENIX (39). For more details see *SI Materials and Methods* and Table S1.

Solid-State NMR Spectroscopy. Samples were prepared by dissolving 4 mg of peptide and ~30 mg of lipid in TFE/water 50/50 vol/vol, dried in air and under high vacuum, applied onto 20 ultra-thin cover glasses, and equilibrated at 93% relative humidity, as described previously (45). Where appropriate, $ZnCl_2$ was added in five- to ten-fold molar excess over the peptide. As an alternate, peptide and $ZnCl_2$ were added to preformed vesicles, and the resulting mixture was applied onto the glass plates (45). The ss-NMR spectra were recorded on a Bruker Avance wide-bore NMR spectrometer operating at 9.4 T with flat-coil probes as described previously (46). Orientational restraints were calculated from the solid-state NMR spectra as described in (46) by using the chemical shift tensor (44, 65, 211) ppm, a maximum quadrupolar splitting of 74 kHz for the alanine ^2H_3C group and DCD coordinates from the crystal structure. For further details of ss-NMR methods and data analysis see *SI Materials and Methods*.

Electrophysiology. Giant unilamellar vesicles (GUVs) composed of DPhPC/cholesterol (9:1) were prepared by the electroformation method with a 3-V peak-to-peak AC voltage at a frequency of 5 Hz for 2 h at 20 °C in the presence of 1 M sorbitol (47–49). A freestanding membrane was prepared by spreading a GUV in 1 M NaCl, 5 mM Hepes, pH 7.1 on an aperture in a borosilicate chip (Port-a-Patch; Nanion Technologies) by applying 15–40-mbar negative pressure resulting in a solvent-free membrane with a resistance in the GΩ range. After successful membrane formation, varying amounts of DCD stock solution (100 μM) were added to 50-μL buffer solution, while applying a DC potential of +100 mV. Current traces were recorded at a sampling rate of 50 kHz using an Axopatch 200B amplifier (Axon Instruments). They were filtered with a low-pass four-pole Bessel filter of 1 kHz and digitized by an A/D converter (Digidata 1322; Axon Instruments). Data evaluation was performed with the pClamp 9 software package (Axon Instruments). For additional details see *SI Materials and Methods*.

Molecular Dynamics and Computational Electrophysiology Simulations. All MD simulations were performed with the GROMACS package, version 4.5 (50) in combination with the CHARMM36 force field (51). Unless otherwise stated, the simulation temperature was 310 K. The protein, lipids, and water/ions

were coupled separately to a temperature bath with the v-rescale method with a time constant of 0.1 ps (52). Short-range electrostatics were calculated with a cutoff of 1.3 nm. Long-range electrostatics were treated with the particle-mesh Ewald method (53). Short-range Van der Waals (VdW) interactions were calculated explicitly up to a distance of 0.8 nm, beyond which a switch function was used to smoothly switch off the VdW interactions to reach 0 at 1.2 nm. All bonds were constrained using the LINCS method (54). The time step was 2 fs for all-atom MD simulations and 4 fs for simulations with the virtual site model for hydrogen atoms (55), respectively. To study whether the oligomer is ion conductive, we used the computational electrophysiology method (26). For additional details see *SI Materials and Methods*.

ACKNOWLEDGMENTS. We thank Mike E. Cates, Cait MacPhee, and Gerhard Wagner for reading the manuscript critically and Robert Schneider for helpful discussions. We also thank Reinhard Albrecht for crystallization of the peptides and Matt Carr for the peptide–peptide docking. The help of the beamline staff of PXII (Swiss Light Source, Switzerland) is greatly acknowledged. This work was supported by the Max Planck Society, the Agence Nationale de la Recherche (Laboratory of Excellence: Chemistry of Complex Systems), the International Center for Frontier Research in Chemistry, Strasbourg, and Ikerbasque Research Foundation. C. Song was supported by the Alexander von Humboldt Foundation. U.Z. acknowledges the Scottish Universities Physics Alliance and the UK National Physical Laboratory for funding. C.W., C. Steinem, and B.L.d.G. thank the German Research Foundation, Sonderforschungsbereich 803 for financial support.

1. Zasloff M (2002) Antimicrobial peptides of multicellular organisms. *Nature* 415(6870): 389–395.
2. Hancock RE, Diamond G (2000) The role of cationic antimicrobial peptides in innate host defences. *Trends Microbiol* 8(9):402–410.
3. Peschel A, Sahl H-G (2006) The co-evolution of host cationic antimicrobial peptides and microbial resistance. *Nat Rev Microbiol* 4(7):529–536.
4. Fjell CD, Hiss JA, Hancock REW, Schneider G (2012) Designing antimicrobial peptides: Form follows function. *Nat Rev Drug Discovery* 11(1):37–51.
5. Hancock REW, Sahl H-G (2006) Antimicrobial and host-defense peptides as new anti-infective therapeutic strategies. *Nat Biotechnol* 24(12):1551–1557.
6. Spellberg B, et al.; Infectious Diseases Society of America (2008) The epidemic of antibiotic-resistant infections: A call to action for the medical community from the Infectious Diseases Society of America. *Clin Infect Dis* 46(2):155–164.
7. Bush K, et al. (2011) Tackling antibiotic resistance. *Nat Rev Microbiol* 9(12):894–896.
8. Hersh AL, Chambers HF, Maselli JH, Gonzales R (2008) National trends in ambulatory visits and antibiotic prescribing for skin and soft-tissue infections. *Arch Intern Med* 168(14):1585–1591.
9. Brogden KA (2005) Antimicrobial peptides: Pore formers or metabolic inhibitors in bacteria? *Nat Rev Microbiol* 3(3):238–250.
10. Melo MN, Ferre R, Castanho MA (2009) Antimicrobial peptides: Linking partition, activity and high membrane-bound concentrations. *Nat Rev Microbiol* 7(3):245–250.
11. Arouri A, Dathe M, Blume A (2009) Peptide induced demixing in PG/PE lipid mixtures: A mechanism for the specificity of antimicrobial peptides towards bacterial membranes? *Biochim Biophys Acta* 1788(3):650–659.
12. Gläser R, et al. (2005) Antimicrobial psoriasin (S100A7) protects human skin from Escherichia coli infection. *Nat Immunol* 6(1):57–64.
13. Schittek B, et al. (2001) Dermcidin: A novel human antibiotic peptide secreted by sweat glands. *Nat Immunol* 2(12):1133–1137.
14. Ganz T (2003) Defensins: Antimicrobial peptides of innate immunity. *Nat Rev Immunol* 3(9):710–720.
15. Bardan A, Nizet V, Gallo RL (2004) Antimicrobial peptides and the skin. *Expert Opin Biol Ther* 4(4):543–549.
16. Paulmann M, et al. (2012) Structure-activity analysis of the dermcidin-derived peptide DCD-1L, an anionic antimicrobial peptide present in human sweat. *J Biol Chem* 287 (11):8434–8443.
17. Cipáková I, Gasperík J, Hostinová E (2006) Expression and purification of human antimicrobial peptide, dermcidin, in Escherichia coli. *Protein Expr Purif* 45(2):269–274.
18. Brogden KA, De Lucca AJ, Bland J, Elliott S (1996) Isolation of an ovine pulmonary surfactant-associated anionic peptide bactericidal for Pasteurella haemolytica. *Proc Natl Acad Sci USA* 93(1):412–416.
19. Eissa A, Amodeo V, Smith CR, Diamandis EP (2011) Kallikrein-related peptidase-8 (KLK8) is an active serine protease in human epidermis and sweat and is involved in a skin barrier proteolytic cascade. *J Biol Chem* 286(1):687–706.
20. Hessa T, et al. (2005) Recognition of transmembrane helices by the endoplasmic reticulum translocon. *Nature* 433(7024):377–381.
21. Hessa T, et al. (2007) Molecular code for transmembrane-helix recognition by the Sec61 translocon. *Nature* 450(7172):1026–1030.
22. Bechinger B, Sizun C (2003) Alignment and structural analysis of membrane polypeptides by15N and31P solid-state NMR spectroscopy. *Concepts Magn Reson* 18A: 130–145.
23. Bechinger B, Resende JM, Aisenbrey C (2011) The structural and topological analysis of membrane-associated polypeptides by oriented solid-state NMR spectroscopy: Established concepts and novel developments. *Biophys Chem* 153(2-3):115–125.
24. Murzyn K, Róg T, Pasenkiewicz-Gierula M (2005) Phosphatidylethanolamine-phosphatidylglycerol bilayer as a model of the inner bacterial membrane. *Biophys J* 88(2): 1091–1103.
25. Yang B, Verkman AS (1997) Water and glycerol permeabilities of aquaporins 1-5 and MIP determined quantitatively by expression of epitope-tagged constructs in Xenopus oocytes. *J Biol Chem* 272(26):16140–16146.
26. Kutzner C, Grubmüller H, de Groot BL, Zachariae U (2011) Computational electrophysiology: The molecular dynamics of ion channel permeation and selectivity in atomistic detail. *Biophys J* 101(4):809–817.
27. Hill CP, Yee J, Selsted ME, Eisenberg D (1991) Crystal structure of defensin HNP-3, an amphiphilic dimer: Mechanisms of membrane permeabilization. *Science* 251(5000): 1481–1485.
28. Terwilliger TC, Weissman L, Eisenberg D (1982) The structure of melittin in the form I crystals and its implication for melittin's lytic and surface activities. *Biophys J* 37(1): 353–361.
29. Langs DA (1988) Three-dimensional structure at 0.86 A of the uncomplexed form of the transmembrane ion channel peptide gramicidin A. *Science* 241(4862):188–191.
30. Bechinger B (1997) Structure and functions of channel-forming peptides: Magainins, cecropins, melittin and alamethicin. *J Membr Biol* 156(3):197–211.
31. Fox RO, Jr., Richards FM (1982) A voltage-gated ion channel model inferred from the crystal structure of alamethicin at 1.5-A resolution. *Nature* 300(5890):325–330.
32. Roux B (2002) Theoretical and computational models of ion channels. *Curr Opin Struct Biol* 12(2):182–189.
33. Christensen B, Fink J, Merrifield RB, Mauzerall D (1988) Channel-forming properties of cecropins and related model compounds incorporated into planar lipid membranes. *Proc Natl Acad Sci USA* 85(14):5072–5076.
34. Kagan BL, Selsted ME, Ganz T, Lehrer RI (1990) Antimicrobial defensin peptides form voltage-dependent ion-permeable channels in planar lipid bilayer membranes. *Proc Natl Acad Sci USA* 87(1):210–214.
35. Bechinger B (2011) Insights into the mechanisms of action of host defence peptides from biophysical and structural investigations. *J Pept Sci* 17(5):306–314.
36. Bechinger B, Lohner K (2006) Detergent-like actions of linear amphipathic cationic antimicrobial peptides. *Biochim Biophys Acta* 1758(9):1529–1539.
37. Kralj JM, Hochbaum DR, Douglass AD, Cohen AE (2011) Electrical spiking in Escherichia coli probed with a fluorescent voltage-indicating protein. *Science* 333(6040): 345–348.
38. Kabsch W (2010) Integration, scaling, space-group assignment and post-refinement. *Acta Crystallogr D Biol Crystallogr* 66(Pt 2):133–144.
39. Adams PD, et al. (2011) The Phenix software for automated determination of macromolecular structures. *Methods* 55(1):94–106.
40. Zwart PH, et al. (2008) Automated structure solution with the PHENIX suite. *Methods Mol Biol* 426:419–435.
41. Winn MD, et al. (2011) Overview of the CCP4 suite and current developments. *Acta Crystallogr D Biol Crystallogr* 67(Pt 4):235–242.
42. Cowtan K (2006) The Buccaneer software for automated model building. 1. Tracing protein chains. *Acta Crystallogr D Biol Crystallogr* 62(Pt 9):1002–1011.
43. Emsley P, Lohkamp B, Scott WG, Cowtan K (2010) Features and development of Coot. *Acta Crystallogr D Biol Crystallogr* 66(Pt 4):486–501.
44. Murshudov GN, et al. (2011) REFMAC5 for the refinement of macromolecular crystal structures. *Acta Crystallogr D Biol Crystallogr* 67(Pt 4):355–367.
45. Aisenbrey C, Bertani P, Bechinger B (2010) Solid-state NMR investigations of membrane-associated antimicrobial peptides. *Methods Mol Biol* 618:209–233.
46. Michalek M, Salnikov ES, Werten S, Bechinger B (2013) Membrane interactions of the amphipathic amino-terminus of huntingtin. *Biochemistry* 52(5):847–858.
47. Angelova MI, Dimitrov DS (1986) Liposome electroformation. *Faraday Discuss Chem Soc* 81:303–311.
48. Angelova M, Dimitrov D (1988) A mechanism of liposome electroformation. *Trends in Colloid and Interface Science II*, ed Degiorgio V (Springer, Berlin), pp 59–67.
49. Angelova M (2000) Giant vesicles. *Perspectives in Supramolecular Chemistry*, eds Luisi PL, Walde P (Wiley-Interscience, Chichester, UK), 1st Ed, pp 27–36.
50. Hess B, Kutzner C, Van der Spoel D, Lindahl E (2008) GROMACS 4: Algorithms for highly efficient, load-balanced, and scalable molecular simulation. *J Chem Theory Comput* 4:435–447.
51. Klauda JB, et al. (2010) Update of the CHARMM all-atom additive force field for lipids: Validation on six lipid types. *J Phys Chem B* 114(23):7830–7843.
52. Bussi G, Donadio D, Parrinello M (2007) Canonical sampling through velocity rescaling. *J Chem Phys* 126(1):014101.
53. Essmann U, et al. (1995) A smooth particle mesh Ewald method. *J Chem Phys* 103: 8577–8593.
54. Hess B, Bekker H, Berendsen HJC, Fraaije JGEM (1997) LINCS: A linear constraint solver for molecular simulations. *J Comput Chem* 18:1463–1472.
55. Feenstra KA, Hess B, Berendsen HJC (1999) Improving efficiency of large time-scale molecular dynamics simulations of hydrogen-rich systems. *J Comput Chem* 20: 786–798.